Quantification of the morphology of gold grains in 3D using X-ray microscopy and SEM photogrammetry

François-Xavier Masson[1*], Georges Beaudoin[1*] and Denis Laurendeau[2*]

[1] Université Laval, Department of Geology and Geological Engineering, Québec, QC, Canada.

[2] Université Laval, Department of Electrical and Computer Engineering, Québec, QC, Canada.

** Centre de recherche sur la géologie et l'ingénierie des ressources minérales (E4m).*

ABSTRACT: The shape of gold is widely used in mineral exploration and in sedimentology to estimate the distance of transport from the source to the site of deposition. However, the estimation of the morphology is based on qualitative observations or on the quantification of the shape in 2D. The 3D analysis of the grain shape is useful for accurate morphometric quantification and to evaluate its volume, which is related to the particle size. This study compares the X-ray 3D microscope and 3D SEM photogrammetry to reconstruct the shape of gold particles. These new methods are exploited to quantify the shape of gold grains 85 to 300 µm in size. The shape parameters, such as axial lengths, surface area, volume, diameter of curvature of all corners, and diameter of the largest inscribed sphere and smallest circumscribed sphere are measured on a particle in order to estimate shape factors such as the flatness ratios, the shape indexes, the sphericity, and the roundness. Most of shape parameters and shape factors estimated on the same gold grain with simple geometry are similar between the two approaches. This result validates these methods for the 3D description of gold particles with simple morphology, while providing a methodology for describing grains with more complex geometry.

INTRODUCTION

In detrital environments, the shape of a gold grain is commonly used for mineral exploration (Giusti 1986; Hérail 1988; Grant et al. 1991; Minter et al. 1993; Averill 2001; Townley et al. 2003), but grain description remains qualitative and subjective. It is accepted that the shape of a gold grain provides information about the distance of transport relative to the source (Hallbauer and Utter 1977; Hérail et al. 1990; Dilabio 1991; Knight et al. 1999; Averill 2001; Townley et al. 2003; Craw et al. 2017; Kerr et al. 2017). The evolution of gold-grains morphology is used to estimate the distance of transport from the primary source in various surficial deposits (Hérail et al. 1989; Youngson and Craw 1999; McClenaghan 2001; Craw et al. 2017).

In the fluvial environment, some authors have used the flatness index (Wentworth 1922; Cailleux 1945) and the Corey Shape Factor (Corey 1949) to quantify the particle flatness as a proxy of the distance of transport of the gold grain (Giusti 1986; Hérail et al. 1990; Youngson and Craw 1999; Townley et al. 2003; Barrios et al. 2015). However, for glacial and eolian environments, the classification depends on the shape and the surface texture of gold grains determined by scanning electron microscope (SEM) observation (DiLabio 1990; Minter et al. 1993; Smith et al. 1993). In sedimentology, additional factors are used to quantify a particle shape (Blott and Pye 2008). The sphericity is commonly calculated using the three principal axes to yield the intercept sphericity (Krumbein 1941), the maximum sphericity (Folk 1955; Sneed and Folk 1958), and the working sphericity (Aschenbrenner 1956). Some sphericity factors are calculated using the ratio of the diameter of the largest inscribed circle to the diameter of the smallest circumscribed circle (Wadell 1933; Aschenbrenner 1956) or using the volume and surface area of the particle (Wadell 1932; Aschenbrenner 1956). Other factors such as the Janke (1966), Williams (1965), Aschenbrenner (1956), and oblate-prolate (Dobkins and Folk 1970) form factors help describe particle morphology. According to Blott and Pye (2008), the most representative value of roundness and angularity is estimated using the average ratio of the diameter of curvature of all corners and the diameter of the largest inscribed circle (Wadell 1932).

The physical characteristics, especially the malleability, of natural gold grains can yield a complex shape, and the quantification of the morphology remains problematic in two dimensions (2D). A 2D characterization of the shape of gold grains can be performed using software tools (Crawford and Mortensen 2009). The SEM image scale is approximate and overlooks the topographic variations at the surface of the grain such that the estimation of 2D measurements is not accurate. The thickness of a particle is used in many shape-factor estimates, and this parameter is difficult to quantify on 2D images with binocular-microscope or SEM images. Three-dimensional (3D) quantification provides a better way to estimate shape factors. In addition, the volume of a grain, quantified in 3D, is the only parameter unaffected by the shape of the grain; unlike the long axis, for example, it can thus give an accurate estimate of the particle "size" (Wadell 1932). In addition, 2D characterization covers a particle's visible surface, and the results can differ from one face to another, especially for malleable gold grains. The 3D methods are therefore necessary to measure the particle dimensions with greater precision, the surface area and the volume.

This study presents two methods to quantify the shape of gold grains using 3D reconstructions: (1) 3D high-resolution X-ray microscopy (XRM); and (2) SEM photogrammetry to produce a 3D mesh of the grain shape. Both methods yield measurements such as triaxial lengths, surface area, and volume that can be used to quantify particle shape factors, which are compared to four gold grains recovered from fluvial, glacial, and aeolian sediments.

METHODS

Shape Factors

In sedimentary environments, morphological factors are used to characterize and classify particle shape (Table 1). These morphological features were defined in 2D and were applied in 3D through the development of image processing, but it remains complicated to evaluate them accurately (Blott and Pye 2008). Many shape factors are based on the long (L), intermediate (I), and short (S) axes, considering L > I > S, where each is orthogonal to the other two axes. The Wentworth flatness index (Wentworth 1922), also called Cailleux flatness index (Cailleux 1945), is commonly used for the characterization and classification of particle flatness in fluvial environments. The Corey shape factor is also used to describe flatness in alluvial particles (Giusti 1986; Barrios et al. 2015). The Janke form factor (Janke 1966) is related to a flatness ratio and yields results similar to those of the Corey shape factor. The Aschenbrenner (Aschenbrenner 1956) and the Williams (Williams 1965) shape factors are based on the degree of flatness (S/I) and elongation (I/L) to describe disk-like or rod-like particles, while the Oblate-Prolate index proposed by Dobkins and Folk (1970) is based on the degree of equancy (S/L), to describe platy and elongate particle. The Krumbein intercept sphericity (Krumbein 1941), the Folk maximum projection sphericity (Folk 1955), and the Aschenbrenner working sphericity (Aschenbrenner 1956) are generally used to quantify sphericity using the dimensions of the particle. The degree of true sphericity proposed by Wadell (1932) is based on the particle volume (V) and the surface area (A). This factor is considered the most accurate estimate of sphericity (Wadell 1932). Wadell (1933) suggested a formula for operational sphericity using the volumes as described by Aschenbrenner (1956). Riley (1941) suggested to measure the diameters of the largest inscribed and the smallest circumscribed circles to yield a circularity value in 2D, which can be used in 3D as a proxy for sphericity (Blott and Pye 2008). The roundness value of Wadell (1932) is based on the diameter of the largest inscribed circle and the diameter of curvature at all corners of the particle.

Gold Grains

Various shape of gold grains from various sedimentary deposits were compared in this study: (1) gold grain 1 is an elongated block and has a simple geometry. It comes from fluvial sediments and was collected with a prospecting pan; (2) gold grain 2 is well rounded and has a cavity on its surface. It was collected in glacial sediments and extracted by mineral separation; (3) gold grain 3 has complex geometry and is curled up. It was collected under the same conditions as grain 2; (4) gold grain 4 is a flat particle with a smooth surface texture; it was collected in eolian sediments and extracted by mineral separation. Grain 1 is considered as a reference gold grain, and the methodology is described for this one. The guideline is consistent for the analysis of other grains; however, some software parameters may vary depending on the nature and positioning of the particle.

3D X-ray Microscope

In this study, a Xradia 520 Versa X-ray microscope (Carl Zeiss AG) was used to scan gold grains to quantitatively reconstruct their shape in 3D. X-ray tomography is non-destructive and splices the grain perpendicular to the spinning axis. The gold grain is placed in a plastic tube filled with silica powder to maintain it in the middle part of the tube and enable the grain to be recovered after analysis. The matrix supporting the gold grain must be stable and strong enough so that the grain remains immobile in order to reduce noise during scanning. For this study, an X-ray energy of 140.1 keV, a current of 68.9 μA, and a LE6 filter placed between the sample and the source are used in order to penetrate the dense gold grain. A total of 3,201 projections are required to obtain high-contrast images. The exposure time is set at 2 seconds to minimize processing time. The grain is turned for 360° and the detector measures X-ray absorption. A 4x optical magnification yields a spatial resolution of 0.73 μm. A set of 1,983 grayscale density-contrast images are produced, which represent the image of the grain slices. Dragonfly (Object Research Systems), a quantitative visualization software, was used to create a model of the particle in 3D, according to the grayscale apparent-density images.

The apparent density of gold grain 1 ranges from 0 to 60,076. These values change according to the experimental conditions in addition to the target density. The dataset consists of three classes (Fig. 1A): (1) the background noise, composed of air, forms 4.72% of the dataset and has a density value ranging from 0 to 10,279; (2) the silica matrix that holds the gold grain is represented by 71.89% of the dataset, with a density value ranging from 10,279 to 37,770; (3) the gold grain forms 23.39% of the dataset with a density value ranging from 37,770 to 60,076. In order to define the boundary of the object, it is necessary to set a minimum density value as the transition between silica and gold (Fig. 1A). The minimal density of gold for this dataset is set to 37,770, such that higher density values are assumed to belong to the gold particle (Fig. 1A). Dragonfly ORS reconstructs the grain in 3D with a gold boundary at apparent density of 37,770 and up to 60,076 (Fig. 1B). The background noise and the silica matrix are thus removed from this 3D model to yield the particle shape (Fig. 1B). The grain can be sliced in planes to analyze cross sections and generate a density profile through the grain (Fig. 1C). The profile shows the apparent-density values across the boundary between silica and gold (Fig. 1D). The gold density values are roughly of 50,000, and a drop of apparent density inside the grain indicates a void or heterogeneity in the particle (Fig. 1D). Finally, a region of interest is determined by the apparent density of gold grain, and a normal mesh is produced. A Laplacian smoothing filter (one iteration) is used to remove the noise on this mesh while maintaining its roughness.

MeshLab (Cignoni et al. 2008) is used to obtain the surface area, the volume, and the long, intermediate, and short axes of the grain. A minimal bounding box that contains the particle is acquired by rotation, and translation, and the dimensions of this box are correlated to the axes of the grain. To estimate the maximum length axis, the mesh is imported into the PolyWorks inspection software (InnovMetric), which is used to compare the normal direction for each point of the polygonal mesh. The software produces a thickness map along the whole grain. The length is calculated according to the maximum distance between two surfaces of opposite orientations. The MATLAB package entitled *A suite of minimal bounding objects* (D'Errico 2014) is used to measure the diameter of the largest inscribed sphere, and the package entitled *Exact minimum bounding spheres and circles* (Semechko 2019) is used to obtain the diameter of the smallest circumscribed sphere. The MATLAB package entitled *Particle Roundness and Sphericity Computation* (Zheng and Hryciw 2015) is used to fit circles on the particle corners and yields a value for roundness on mesh projections in 2D, based on Wadell's formula. The script parameters (tol = 0.3, factor = 0.98, span = 0.07) were kept constant as well as XRM mesh outlines so as not to influence the measurements.

3D SEM and Photogrammetry

Photogrammetry was used to reconstruct the 3D shape of nanoscale particles from SEM images (Gontard et al. 2016). The same process is used to reconstruct the morphology of microscopic gold grains (Fig. 2). A SEM Quanta-3D-FEG (FEI) was used to capture secondary-electron images of gold grains. Grain 1 surface texture is captured with SEM using a secondary-electron detector and a magnification of a striated surface (Fig. 2A). Sample preparation consists in placing the grain at the top of a wood stick on carbon tape, in order to have a conductive setup for high-quality secondary-electron images. For this study, the energy is set at 3 keV to yield highest resolution surface texture, at constant magnification of x500. In order to document the surface close to the stage for efficient 3D representation of each face of the grain, the stage is tilted at 70°. The grain is rotated for 360° with 18° steps, which yields 20 images, the minimum required for volume reconstruction. Overlap is necessary between image pairs for photogrammetric reconstruction. With more matching points, the software stitches the mesh object with better precision and increased textural details. We tested photogrammetry software tools, such as VisualSFM (Wu 2011) and COLMAP (Schönberger et al. 2016), but those software package could not reconstruct the grain from SEM images and the results were not replicable. ReCap Photo (Autodesk) was able to achieve efficient reconstruction of the particle volume with surface textures. ReCap Photo proceeds to the 3D reconstruction using 19 camera views from SEM images. After reconstruction, a 3D mesh is produced with surface textures (Fig. 2B). However, SEM images do not contain information on focal length, and this results in the loss of absolute scale on the mesh produced by ReCap Photo. To recover absolute scale, the model is calibrated from a SEM reference image. Measurements are taken on this reference image, for which the scale is known, and then applied in the grain model. The magnification of the SEM striated surface image of gold grain 1 can be observed easily on the reconstruction (Fig. 2A). To calibrate the model, we took five measurements, and the average value is used for scale calibration with standard deviations of (1) 2.1% for the axial length; (2) 6.2% for the volume; (3) 4.1% for the surface area. ReCap Photo offer tools that enable the sample stage to be removed from the model by deleting mesh triangles (Fig. 2C). However, this creates a hole in the mesh. To fill this hole, we added a flat mesh at the base of the model to enable estimation of the volume of the particle. Finally, the mesh is aligned with the origin (Fig. 2D).

The same data processing used for microtomography is used to obtain the axial lengths, the surface area, the volume, the diameter of the largest inscribed sphere, the diameter of the smallest circumscribed sphere, and the computation of the roundness value of the gold grain.

RESULTS

Estimates of Shape Parameters

The 3D XRM mesh of grain 1 was imported in MeshLab to measure the minimal bounding-box dimensions (L, I, S), the surface area and the volume (Fig. 3A). PolyWorks yields a maximum axis length and the volume of the circumscribed sphere (Fig. 3B). The thickness map indicates an anomaly in the particle with variations of the thickness detected on the surface. This anomaly suggests the presence of a void or an inclusion at 0 to 25 µm depth (Fig. 3B). The MATLAB packages produce the diameter of the largest inscribed sphere and the diameter of the smallest circumscribed sphere (Fig. 3C), based on the convex hull of the particle. The Wadell roundness was calculated with the MATLAB algorithm on six projection planes (X, -X, Y, -Y, Z, -Z) of the particle (Fig. 3D). The 3D SEM particle reconstruction of grain 1 was imported in MeshLab in order to measure the minimal bounding-box dimensions, the surface area, and the volume (Fig. 4A). PolyWorks yields measurement of the maximum axis length and the volume of the circumscribed sphere (Fig. 4B). The MATLAB packages are used to provide the diameter of the largest inscribed sphere and the smallest circumscribed sphere on the convex hull of the grain (Fig. 4C). The Wadell roundness was calculated on the six projection planes of the particle (Fig. 4D). Average shape parameters and standard deviation on grain 1 show that the difference between both methods is less than 6% (Table 2).

The shape parameters were computed for the other gold grains with different geometry (Fig. 5). The reconstruction models for grain 2 yield similar results, but the heterogeneity on the surface reconstructed by the SEM mesh was not captured on the XRM mesh (Fig. 5A). Shape parameters affected by the particle geometry lead to differences between the two methods of 10.2% to 24.2% (Table 2). The grain 3 reconstruction models show slightly different results. The complexity of the grain geometry adds volume at the base of the SEM mesh reconstruction (Fig. 5B). The maximum length of the XRM mesh is smaller than the long-axis measurement, so the volume of the smallest circumscribed sphere is estimated with the value of the long axis. The surface area and the volume of grain 3 vary significantly (Table 2). Grain 4 is flat, and the part in contact with the carbon tape cannot be measured by SEM photogrammetry such that it is not represented well on the SEM model (Fig. 5C). Similar to grain 3, the maximum length of the SEM mesh is smaller than the long-axis measurement. Shape parameters affected by flat particle have differences range between 10.2% and 22.5% (Table 2).

Estimates of Shape Factors

The shape factors are estimated from the shape parameters according to XRM and SEM photogrammetry results (Table 3). The Wadell roundness corresponds to the average value of the six projection planes. For grain 1, the two methods show a difference on the computed shape factors less than 6%, with the exception of the Williams shape factor, the Oblate-Prolate index, and the Wadell roundness, with a difference of 23.1%, 20.1%, and 8.5%, respectively (Table 3). The classification proposed by Blott and Pye (2008), based on the degree of flatness, the degree of elongation, and the degree of equancy, indicates that grain 1 is slightly flat, moderately elongated, and moderately non-equant for SEM results. XRM results show a slightly flat, slightly elongated, and moderately non-equant particle. The flatness indexes are generally similar for the two methods and illustrate a moderately to slightly flat particle. The Aschenbrenner, the Williams, and the Oblate-Prolate factors indicate that the particle is prolate (rod-like). The Krumbein intercept sphericity, the maximum projection sphericity, the degree of true sphericity, and the inscribed circle sphericity indicate that the particle is moderately spherical. However, the operational sphericity has lower values and corresponds to a low-sphericity particle. The Aschenbrenner working sphericity suggests a greater value associated with high-sphericity grain. The Wadell roundness suggests that grain 1 is subrounded for both methods.

The other grains, having a complex geometry, show larger differences between the two methods (Table 3). For these grains, the Williams shape factor and the Oblate-Prolate index have differences up to 30.0% and 294.4%, respectively. The Wadell roundness has a difference up to 19.6%. The MATLAB algorithm was not applied on grains 3 and 4 for two projection planes because of their uncertain boundaries. Other shape factors that have difference in values larger than 10% are (i) the Aschenbrenner shape factor, for grain 2, (ii) the operational sphericity and the degree of true sphericity, for grain 3 and (iii) the majority of shape factors, for grain 4.

DISCUSSION

Comparison Between the Two 3D Methods

This study presents two 3D methods to quantify the morphology of gold grains. Four particles were used to compare shape parameters in 3D, and grain 1 is considered as a reference for the methodology. The Xradia 520 Versa generates X-rays with high energy that penetrate gold and produces a full 3D reconstruction of grains approximately 85 to 300 μm in size. The model represents the surface morphology and gives information about the core of the grain by detecting voids or inclusions. The disadvantages of this method are: (1) the apparent-density contrast must be adjusted to circumscribe the grain, and the boundary between the silica matrix and the gold grain is subtle even if this transition zone is not significant, considering the standard deviation of the axial lengths, surface area, and volume measurements obtained in the experiments; (2) some artifacts may distort the scan quality, such as the blurry borders produced by movement of the grain on the rotating base; (3) the resolution of the device is adequate to reconstruct a gold grain greater than 85 μm in long axis. 3D SEM photogrammetry reconstructs the shape of gold grains greater than 20 μm in size with high resolution. The 3 keV energy provides a better surface texture information, which is useful for the reconstruction. The acquisition time (~ 1 h) is faster than the 3D XRM scan (~ 4 h). The disadvantages of this method are: (1) the acquisition of a partial reconstruction mesh, because the base of the grain must be replaced by a flat mesh; (2) the scale calibration needs to be performed with an average accuracy ± 6.2% and depends on the magnification of a small feature of the object; (3) the observer has no control on the mesh produced by ReCap Photo, on the production of the mesh, or on the smoothing process after reconstruction.

Estimates of Morphological Parameters and Factors

Nevertheless, for gold grains with simple geometry, such as gold grain 1, each method enable estimation of the parameters with less than 6% difference of shape parameters (Table 2). For the 3D SEM method, the estimates vary according to the surface placed on the carbon tape and the geometry of the grain, such that errors on the measurement of shape parameters can be greater (Table 2). Grain 1 has a small contact area with the carbon tape, so the error on the volume and the surface area is minimal. For flat and complex geometry grains, the particle should be placed on a tip or a slice, to minimize this area. However, the matching points can be more difficult for the photogrammetric software to reconstruct the particle volume. The difference between the long axis is generally greater than the difference for the intermediate and the short axes. That is because to find the minimal bounding box, the short axis was found first, followed by the intermediate axis, and the long axis is orthogonal to the two above axes. Although the difference in the maximum length is less than 10% for all grains, this measurement remains problematic when it is smaller than the long-axis value, especially when the grain is curved or has a complex geometry. This term affects the volume of the circumscribed sphere parameter and, therefore, the operational sphericity shape factor. In the case of a comparative study with multiple grains, it is recommended to use the diameter of the smallest circumscribed sphere, measured with the convex hull, although it is less accurate than the maximum length axis.

Most of the shape factors of grain 1 have less than 6% difference between the two methods, which confirms their use for grains with simple geometry (Table 3). However, this is not the case for other grains with more complex geometries (Table 3), where the Oblate-Prolate index and the Williams shape factors have a higher difference up to 294.4% and 30.0%, respectively. The large error between the two methods show that the Oblate-Prolate index is not recommended to estimate the shape of gold particles. The Williams shape factor is efficient to approximate an oblate or prolate particle shape and, except for grain 2, the results are similar considering the range of values expected for the factor (Table 1). The same applies for the Aschenbrenner-shape-factor estimates on grains 2 and 4. The Wadell roundness is calculated on six projection planes in 2D. The estimation in 3D is determined by the average result of the sections. This parameter is highly dependent on mesh smoothness, and the results vary according to the projections planes orientations. The meshes are obtained with two different software packages and different degrees of smoothing. In this study, we decided to work with the original mesh, but there is residual roughness on at the boundaries. SEM images with high resolution provide a detailed mesh based on surface texture, which corresponds to the surface roughness, while the resolution of the 3D XRM produces a smooth surface with less detail on the roughness. The MATLAB algorithm is not efficient for complex grain shapes, especially when the boundaries are rough. The roundness differences are influenced by smoothing and the orientation of the projection planes, such that the shape factor is not recommended to estimate the roundness.

The operational sphericity and the degree of true sphericity depend on the volume of the particle. This is a major factor, and the difference is higher to 10%, except for the grain 1 (Table 2). This difference can be correlated with the grain manipulation during the setup change between XRM and SEM. However, the SEM setup can be used for analysis with 3D XRM, which will reduce the number of manipulations and shape modification. The volume, estimated by SEM photogrammetry, is also highly dependent on the surface area placed on the carbon tape, and the estimation remains delicate. It is essential to limit the contact with the carbon tape or to use the XRM method for large complex or flat particles to guarantee an accurate volume measurement.

Comparison of 2D and 3D Analyses

Shape parameters and computed shape factors are estimated in 2D, for gold grain 1, using a SEM image (Fig. 2A) and compared to the 3D SEM results (Table 4). The 2D shape parameters such that the diameter of the largest inscribed circle, the intermediate axis, and the short axis show large differences with the 3D SEM results (Table 4). The short-axis measurement yields the largest difference because it is difficult to measure on a 2D image, even with a large depth of field of the secondary-electron SEM image. The short axis can be estimated using other SEM images from different orientations, to improve the accuracy of measurement of this parameter. The size of the minimal bounding box is highly dependent on the observer's position relative to the sample. Some shape parameters cannot be measured on a 2D image, which limits the amount of computed shape factors that may be relevant to particle-shape quantification (Table 4). The computed shape factors show significant differences between 2D and 3D quantification (Table 4), which are greater than differences of shape factors computed for the two 3D methods (Table 3), except for the Wadell roundness, which is based on 2D projections. 3D analysis provides a more accurate quantification of the commonly used shape factors and of the non-quantifiable factors in 2D, based on the volume, the surface area, and the maximum axis of the particle.

Impact of the Proposed Approaches for Mineral Exploration and Sedimentology

On the one hand, 3D XRM is not a common tool for mineral exploration. On the other hand, the estimates based on 3D SEM presented in this paper are promising for the characterization of particles with simple geometry. Using 3D SEM for the quantification of complex and flat geometries depends on how the grain is placed on the carbon tape. This method can be used to evaluate in 3D the shape of gold grains smaller than 63 μm in size, which typically form 80 to 90% of gold grains in glacial sediments (Averill 2001). The comparison of morphological factors quantified in 3D on detrital gold grains coupled with textural observations is useful to classify the evolution of a malleable gold particle, during transport from the source, in a sedimentary system.

In sedimentology, characterizations of detrital fragments and heavy minerals are used to estimate the distance of transport and provide information about the source of the particles (Wadell 1935). The two methods can provide a quantification of 3D morphology of sedimentary particles and other minerals than gold grains. The 3D estimates can be used to refine degrees of roundness, sphericity, and flatness in order to estimate the distance of transport.

CONCLUSION

The 3D XRM and the SEM coupled with photogrammetry enable the 3D morphology of a gold grain to be reconstructed. For a gold grain with simple geometry, both methods provide similar results on the axial lengths, the surface area, the volume, the diameter of the largest inscribed sphere, and the diameter of the smallest circumscribed sphere, and most of shape factors estimated have less than 6% difference. Quantification of gold grains with a complex geometry, such as flat or curved grains, yield differences between the shape parameters and shape factors that are greater than for grains with a simple geometry, and it varies mainly depending on how the grain is positioned, especially for the SEM method. However, the XRM method produces relevant results to reconstruct the morphology in 3D of a complex gold grain regardless of its orientation. On the one hand, the 3D XRM is more suitable to quantify gold-grain sizes greater than 85 μm and produces full 3D reconstruction. On the other hand, the resolution of the 3D SEM-based method provides a partial reconstruction but allows reconstruction of the 3D shape of particles smaller than 85 μm in size.

ACKNOWLEDGMENTS

We thank Stéphane Gagnon for the data-acquisition analyses with the SEM at Université Laval and Rui Tahara for the data-acquisition analyses with the Xradia 520 Versa at McGill University. Tomographic acquisition was performed using the infrastructure of the Integrated Quantitative Biology Initiative, Canadian Foundation for Innovation Project 33122. The research presented in this paper was funded by the Natural Sciences and Engineering Research Council of Canada (NSERC) collaborative Research and Development grant in partnership with Agnico Eagle Mines Ltd and the Ministère de l'Énergie et des Ressources Naturelles du Québec (MERN).

REFERENCES

Aschenbrenner, B.C., 1956, A new method of expressing particle sphericity: Journal of Sedimentary Petrology, v. 26, p. 15-31.

Autodesk, 2019, ReCap Photo https://www.autodesk.com.

Averill, S.A., 2001, The application of heavy indicator mineralogy in mineral exploration with emphasis on base metal indicators in glaciated metamorphic and plutonic terrains. In: McClenaghan, M.B, Bobrowsky, P.T., Hall, G.E.M. & Cook, S.J. ky, Bobrowsky, P.T., Hall, G.E.M. & Cook, S.J. (eds) Drift Exploration in Glaciated Terrain: Geological Society of London, Special Publication, 185, p. 69-81.

Barrios, S., Merinero, R., Lozano, R., and Orea, I., 2015, Morphogenesis and grain size variation of alluvial gold recovered in auriferous sediments of the Tormes Basin (Iberian Peninsula) using a simple correspondence analysis: Mineralogy and Petrology, v. 109, p. 679-691.

Blott, S.J., and Pye, K., 2008, Particle shape: a review and new methods of characterization and classification: Sedimentology, v. 55, p. 31-63.

Cailleux, A., 1945, Distinction des galets marins et fluviatiles: Société géologique de France, Bulletin, v. 5, p. 375-404.

Cignoni, P., Callieri, M., Corsini, M., Dellepiane, M., Ganovelli, F., and Ranzuglia, G., 2008, Meshlab: an open-source mesh processing tool: Eurographics Italian Chapter Conference, p. 129-136.

Corey, A., 1949, Influence of shape on the fall velocity of sand grains: Colorado A & M College, Fort Collins, unpub: Master's thesis, 102 pp.

Craw, D., Hesson, M., and Kerr, G., 2017, Morphological evolution of gold nuggets in proximal sedimentary environments, southern New Zealand: Ore Geology Reviews, v. 80, p. 784-799.

Crawford, E.C., and Mortensen, J.K., 2009, An ImageJ plugin for the rapid morphological characterization of separated particles and an initial application to placer gold analysis: Computers & Geosciences, v. 35, p. 347-359.

D'Errico, J., 2014, MathWorks : A suite of minimal bounding objects.

DiLabio, R., 1990, Classification and interpretation of the shapes and surface textures of gold grains from till on the Canadian Shield: Geological Survey of Canada, Papers, v. 88, Current Research, Part C, p. 61-65.

Dilabio, R., 1991, Classification and interpretation of the shapes and surface textures of gold grains from till: Gisements alluviaux d'or (Alluvial Gold Placers/Yacimientos aluviales de oro), p. 297-313.

Dobkins, J.E., and Folk, R.L., 1970, Shape development on Tahiti-nui: Journal of Sedimentary Petrology, v. 40, p. 1167-1203.

Dragonfly, [Computer software version 4.0] . Object Research Systems (ORS) Inc, Montreal, Canada, 2019; software available at http://www.theobjects.com/dragonfly.

Folk, R.L., 1955, Student operator error in determination of roundness, sphericity, and grain size: Journal of Sedimentary Petrology, v. 25.

Giusti, L., 1986, The morphology, mineralogy, and behavior of " fine-grained" gold from placer deposits of Alberta: sampling and implications for mineral exploration: Canadian Journal of Earth Sciences, v. 23, p. 1662-1672.

Gontard, L.C., Schierholz, R., Yu, S., Cintas, J., and Dunin-Borkowski, R.E., 2016, Photogrammetry of the three-dimensional shape and texture of a nanoscale particle using scanning electron microscopy and free software: Ultramicroscopy, v. 169, p. 80-88.

Grant, A., Lavin, O., and Nichol, I., 1991, The morphology and chemistry of transported gold grains as an exploration tool: Journal of Geochemical Exploration, v. 40, p. 73-94.

Hallbauer, D., and Utter, T., 1977, Geochemical and morphological characteristics of gold particles from recent river deposits and the fossil placers of the Witwatersrand: Mineralium Deposita, v. 12, p. 293-306.

Hérail, G., 1988, Morphological evolution of supergenetic gold particles: geological significance and interest for mining exploration: C. R. Acad. Sci. Paris, t. 307, Série II, p. 63-69.

Hérail, G., Fornari, M., and Rouhier, M., 1989, Geomorphological control of gold distribution and gold particle evolution in glacial and fluvioglacial placers of the Ancocala-Ananea basin-Southeastern Andes of Peru: Geomorphology, v. 2, p. 369-383.

Hérail, G., Fornari, M., Viscarra, G., and Miranda, V., 1990, Morphological and chemical evolution of gold grains during the formation of a polygenic fluviatile placer: the Mio-Pleistocene Tipuani placer example (Andes, Bolivia): Chronique de la recherche miniere, p. 41-49.

Janke, N., 1966, Effect of shape upon the settling vellocity of regular convex geometric particles: Journal of Sedimentary Petrology, v. 36, p. 370-376.

Kerr, G., Falconer, D., Reith, F., and Craw, D., 2017, Transport-related mylonitic ductile deformation and shape change of alluvial gold, southern New Zealand: Sedimentary Geology, v. 361, p. 52-63.

Knight, J., Morison, S., and Mortensen, J., 1999, The relationship between placer gold particle shape, rimming, and distance of fluvial transport as exemplified by gold from the Klondike District, Yukon Territory, Canada: Economic Geology, v. 94, p. 635-648.

Krumbein, W.C., 1941, Measurement and geological significance of shape and roundness of sedimentary particles: Journal of Sedimentary Petrology, v. 11.

McClenaghan, M.B., 2001, Regional and local-scale gold grain and till geochemical signatures of lode Au deposits in the western Abitibi Greenstone Belt, central Canada. In: McClenaghan, M.B, Bobrowsky, P.T., Hall, G.E.M. & Cook, S.J. ky, Bobrowsky, P.T., Hall, G.E.M. & Cook, S.J. (eds) Drift Exploration in Glaciated Terrain: Geological Society of London, Special Publication, 185, p. 201-224.

Minter, W., Goedhart, M., Knight, J., and Frimmel, H., 1993, Morphology of Witwatersrand gold grains from the Basal Reef; evidence for their detrital origin: Economic Geology, v. 88, p. 237-248.

PolyWorks, 2018, InnovMetric [https://www.innovmetric.com].

Riley, N.A., 1941, Projection Sphericity: Journal of Sedimentary Petrology, v. 11, p. 94-97.

Schönberger, J.L., Zheng, E., Frahm, J.-M., and Pollefeys, M., 2016, Pixelwise view selection for unstructured multi-view stereo: European Conference on Computer Vision, p. 501-518.

Semechko, A., 2019, MathWorks : Exact minimum bounding spheres and circles (https://www.github.com/AntonSemechko/Bounding-Spheres-And-Circles).

Smith, D.B., Theobald, P.K., Shiquan, S., Tianxiang, R., and Zhihui, H., 1993, The Hatu gold anomaly, Xinjiang-Uygur Autonomous Region, China—testing the hypothesis of aeolian transport of gold: Journal of Geochemical Exploration, v. 47, p. 201-216.

Sneed, E.D., and Folk, R.L., 1958, Pebbles in the lower Colorado River, Texas a study in particle morphogenesis: The Journal of Geology, v. 66, p. 114-150.

Townley, B.K., Hérail, G., Maksaev, V., Palacios, C., de Parseval, P., Sepulveda, F., Orellana, R., Rivas, P., and Ulloa, C., 2003, Gold grain morphology and composition as an exploration tool: application to gold exploration in covered areas: Geochemistry: Exploration, Environment, Analysis, v. 3, p. 29-38.

Wadell, H., 1932, Volume, shape, and roundness of rock particles: The Journal of Geology, v. 40, p. 443-451.

Wadell, H., 1933, Sphericity and roundness of rock particles: The Journal of Geology, v. 41, p. 310-331.

Wadell, H., 1935, Volume, shape, and roundness of quartz particles: The Journal of Geology, v. 43, p. 250-280.

Wentworth, C.K., 1922, The shapes of beach pebbles. US Geol. Surv. Prof. Pap., v. 131-C, p. 75-83.

Williams, E.M., 1965, A method of indicating pebble shape with one parameter: Journal of Sedimentary Petrology, v. 35, p. 993-996.

Wu, C., 2011, VisualSFM: A visual structure from motion system: http://ccwu.me/vsfm/.

YOUNGSON, J.H., AND CRAW, D., 1999, Variation in placer style, gold morphology, and gold particle behavior down gravel bed-load rivers: an example from the Shotover/Arrow-Kawarau-Clutha River system, Otago, New Zealand: Economic Geology, v. 94, p. 615-633.

ZHENG, J., AND HRYCIW, R., 2015, Traditional soil particle sphericity, roundness and surface roughness by computational geometry: Géotechnique, v. 65, p. 494-506.

Figure captions

Fig. 1.—**A)** Histogram of apparent density values for the dataset of the gold grain 1. The apparent-density boundary between the background and the silica matrix is at 10,279, whereas the apparent density of the gold grain is set at 37,770. **B)** Gold grain 1 mesh in orthographic projection with three axial planes (X, Y, Z) at apparent density above 37,770. **C**) X, Y, and Z planes that compose the dataset, with a longitudinal transect representation on the X planes. **D)** Apparent density on the 300 μm of the longitudinal transect in the gold grain with a drop of apparent density that corresponds to an inclusion or a void inside the gold grain.

Fig. 2.—**A)** SEM image of the gold grain 1 and magnification of small features for calibration using five measurements (Mi). **B)** Gold grain reconstruction with the sample stage covered by carbon tape and magnification of the same area as in (part A) to calibrate the model with the same five measurements (Mi). **C)** Gold grain after removing base mesh elements and calibration processing. **D)** The model is transformed and closed to fit with the origin of the mesh represented by the grid.

Fig. 3.—Morphological parameters obtained with the 3D X-ray microscope method on the gold grain 1. **A)** MeshLab representation with the minimal bounding box (green) that contains the grain. The software provides measurements of the long axis (L), the intermediate axis (I), the short axis (S), the surface area (A), and the volume (V). **B)** Thickness map representation of the grain obtained with the 3D X-ray microscope (produced by PolyWorks). The red line shows the maximum length axis (M), and the indigo area shows the same inclusion or void as the transect at 0 to 25 μm depth (Fig.1). **C)** Representation of the particle convex hull with the largest inscribed sphere and the smallest circumscribed sphere. The diameter of the smallest circumscribed sphere (Dcs) and the diameter of the largest inscribed sphere (Dis) are measured. **D)** Illustration of six plane sections with the values of the Wadell roundness. The green circles show the curvature of all corners of the particle, and the red circle shows the diameter of the largest inscribed circle.

Fig. 4.—Morphological parameters obtained with the 3D SEM method on the gold grain 1. **A)** MeshLab representation with the minimal bounding box (green) and the measurements of the long axis (L), the intermediate axis (I), the short axis (S), the surface area (A), and the volume (V). **B)** Thickness map of the mesh with the red line showing the maximum axial length (M). **C)** Representation of the convex hull with the largest inscribed sphere and the smallest circumscribed sphere. The diameter of the smallest circumscribed sphere (Dcs) and the diameter of the largest inscribed sphere (Dis) are measured. **D)** Illustration of six plane sections with the values of the Wadell roundness. The green circles show the curvature of all corners of the particle and the red circle shows the diameter of the largest inscribed circle.

Fig. 5.—SEM images, 3D meshes, and shape parameters for SEM and XRM methods: **A)** gold grain 2. The dashed red square shows the heterogeneity on the SEM images and the 3D SEM mesh. **B)** Gold grain 3. **C)** Gold grain 4.

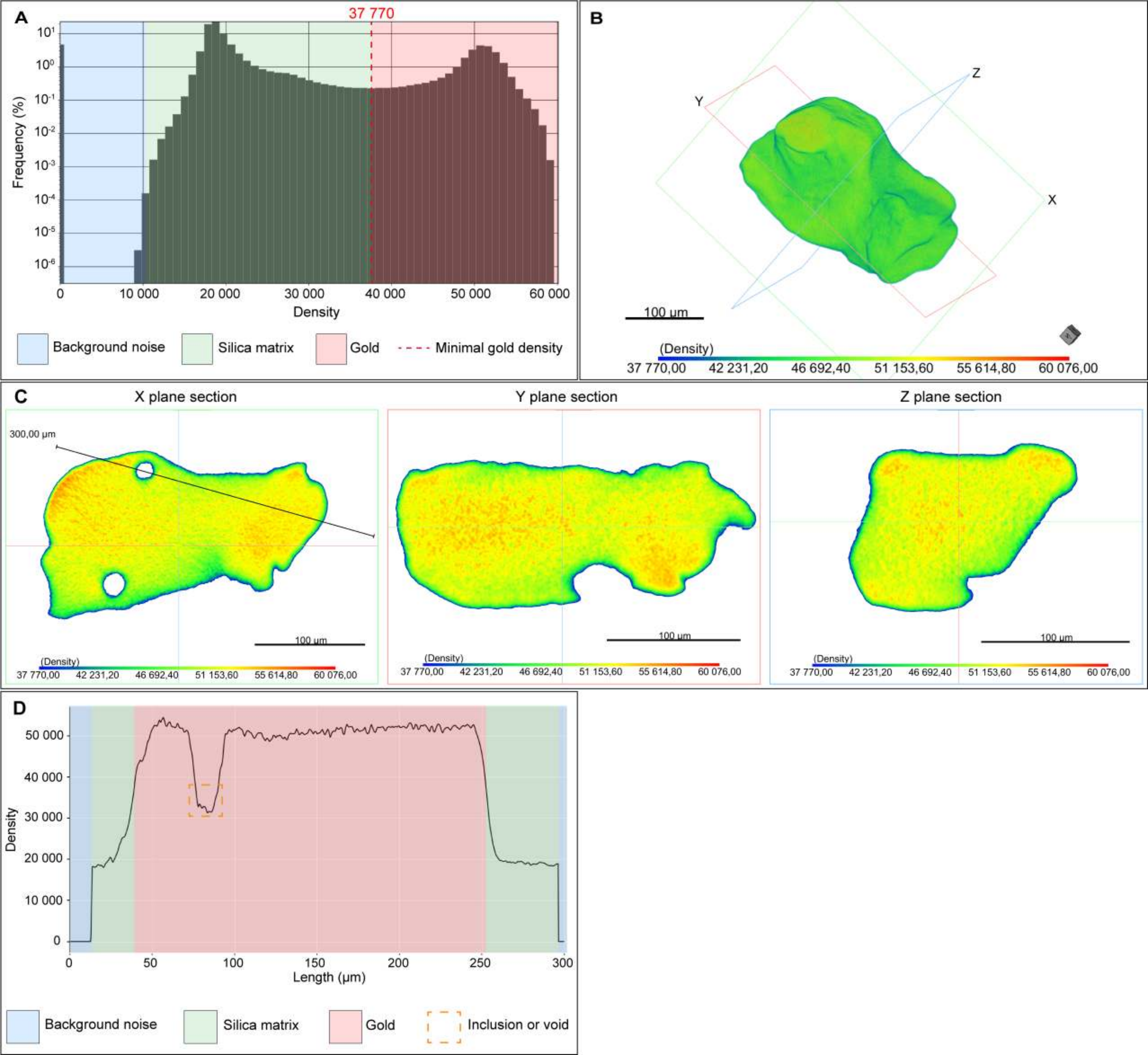

A
37 770
Frequency (%)
Density
Background noise
Silica matrix
Gold
Minimal gold density
B
Z
Y
X
100 µm
(Density)
37 770,00
42 231,20
46 692,40
51 153,60
55 614,80
60 076,00
C
X plane section
Y plane section
Z plane section
300,00 µm
100 µm
D
Density
Length (µm)
Background noise
Silica matrix
Gold
Inclusion or void

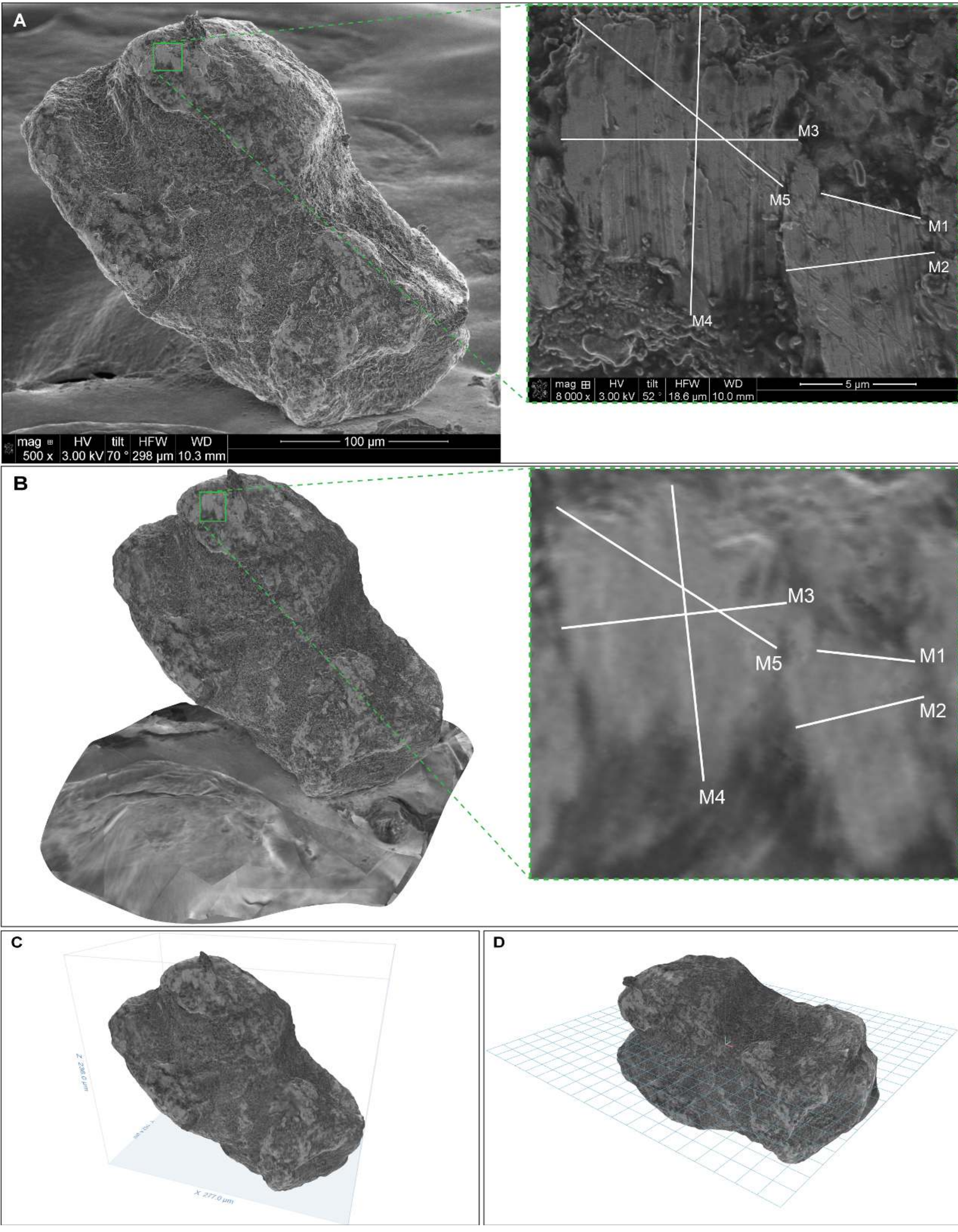
A
mag ⊞ 500 x
HV 3.00 kV
tilt 70 °
HFW 298 µm
WD 10.3 mm
100 µm
M1
M2
M3
M4
M5
mag ⊞ 8 000 x
HV 3.00 kV
tilt 52 °
HFW 18.6 µm
WD 10.0 mm
5 µm
B
M3
M5
M1
M2
M4
C
Z 236.0 µm
X 277.0 µm
D

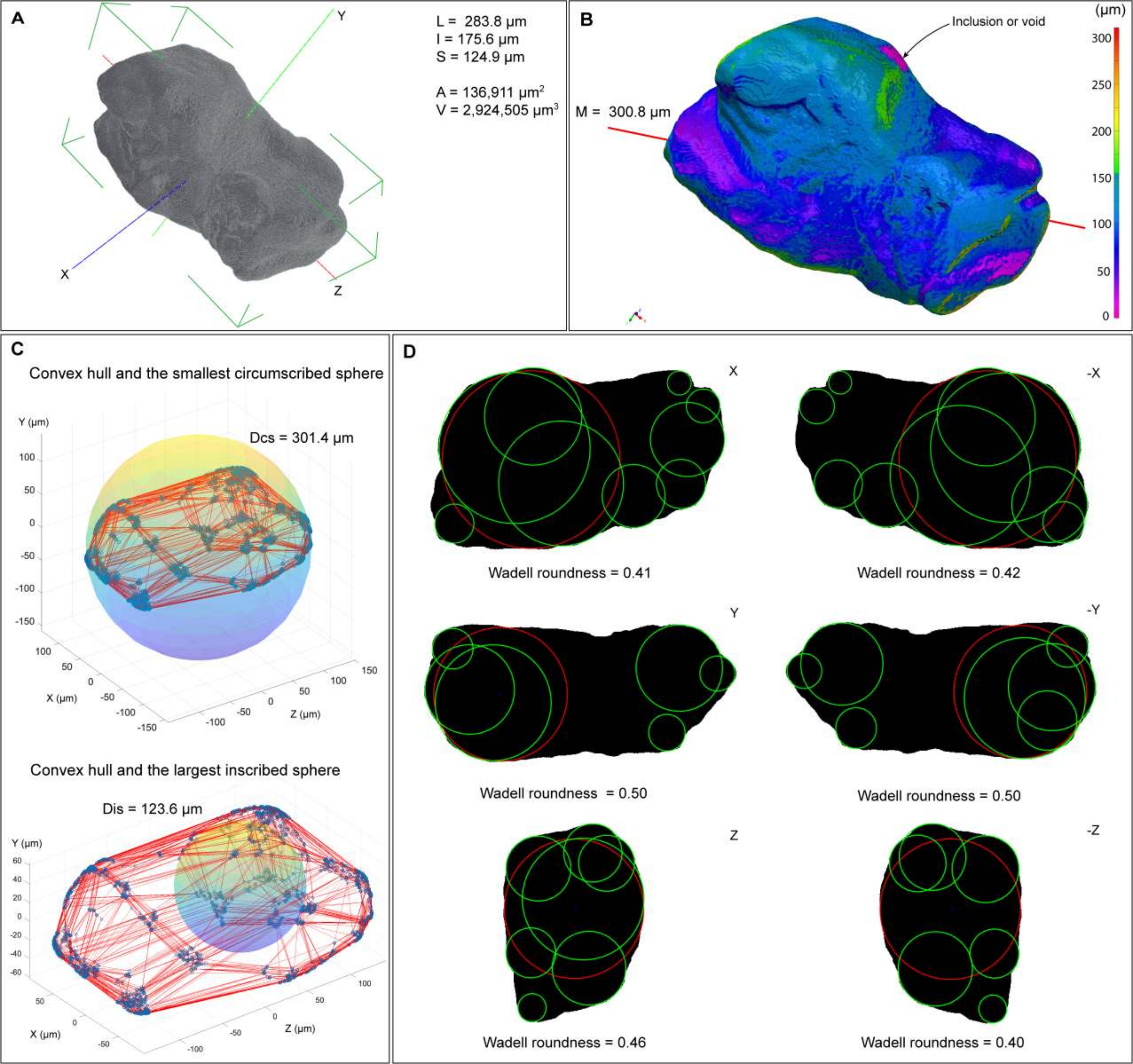
A
L = 283.8 μm
I = 175.6 μm
S = 124.9 μm
A = 136,911 μm2
V = 2,924,505 μm3
X
Y
Z
B
Inclusion or void
M = 300.8 μm
(μm)
300
250
200
150
100
50
0
C
Convex hull and the smallest circumscribed sphere
Dcs = 301.4 μm
Y (μm)
X (μm)
Z (μm)
Convex hull and the largest inscribed sphere
Dis = 123.6 μm
D
X
-X
Wadell roundness = 0.41
Wadell roundness = 0.42
Y
-Y
Wadell roundness = 0.50
Wadell roundness = 0.50
Z
-Z
Wadell roundness = 0.46
Wadell roundness = 0.40

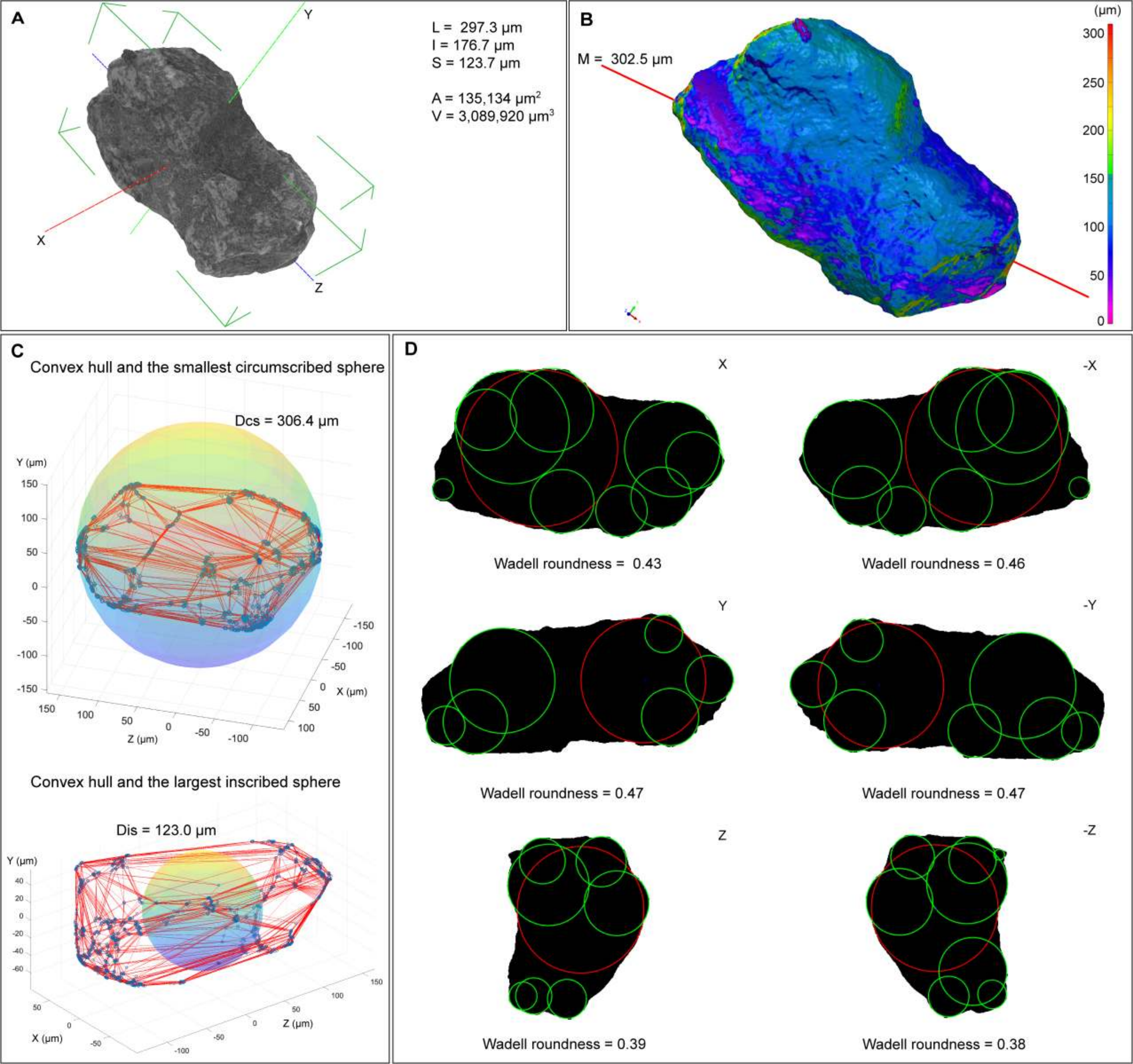
A
L = 297.3 μm
I = 176.7 μm
S = 123.7 μm
A = 135,134 μm2
V = 3,089,920 μm3
X
Y
Z
B
M = 302.5 μm
(μm)
300
250
200
150
100
50
0
C
Convex hull and the smallest circumscribed sphere
Dcs = 306.4 μm
Y (μm)
X (μm)
Z (μm)
Convex hull and the largest inscribed sphere
Dis = 123.0 μm
D
X
-X
Wadell roundness = 0.43
Wadell roundness = 0.46
Y
-Y
Wadell roundness = 0.47
Wadell roundness = 0.47
Z
-Z
Wadell roundness = 0.39
Wadell roundness = 0.38

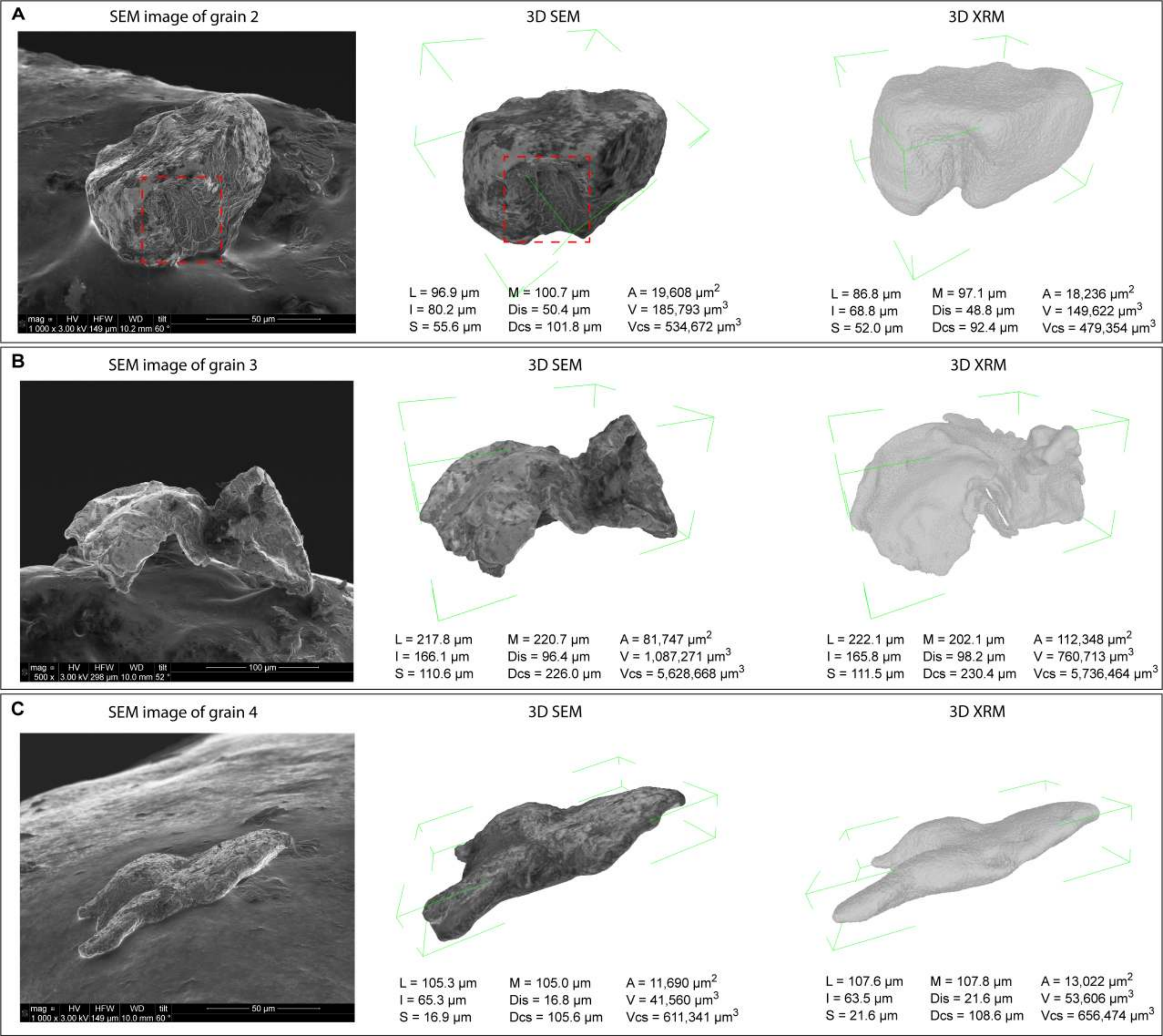
A
SEM image of grain 2
mag HV HFW WD tilt
1 000 x 3.00 kV 149 µm 10.2 mm 60 °
50 µm
3D SEM
L = 96.9 µm
I = 80.2 µm
S = 55.6 µm
M = 100.7 µm
Dis = 50.4 µm
Dcs = 101.8 µm
A = 19,608 µm2
V = 185,793 µm3
Vcs = 534,672 µm3
3D XRM
L = 86.8 µm
I = 68.8 µm
S = 52.0 µm
M = 97.1 µm
Dis = 48.8 µm
Dcs = 92.4 µm
A = 18,236 µm2
V = 149,622 µm3
Vcs = 479,354 µm3
B
SEM image of grain 3
mag HV HFW WD tilt
500 x 3.00 kV 298 µm 10.0 mm 52 °
100 µm
3D SEM
L = 217.8 µm
I = 166.1 µm
S = 110.6 µm
M = 220.7 µm
Dis = 96.4 µm
Dcs = 226.0 µm
A = 81,747 µm2
V = 1,087,271 µm3
Vcs = 5,628,668 µm3
3D XRM
L = 222.1 µm
I = 165.8 µm
S = 111.5 µm
M = 202.1 µm
Dis = 98.2 µm
Dcs = 230.4 µm
A = 112,348 µm2
V = 760,713 µm3
Vcs = 5,736,464 µm3
C
SEM image of grain 4
mag HV HFW WD tilt
1 000 x 3.00 kV 149 µm 10.0 mm 60 °
50 µm
3D SEM
L = 105.3 µm
I = 65.3 µm
S = 16.9 µm
M = 105.0 µm
Dis = 16.8 µm
Dcs = 105.6 µm
A = 11,690 µm2
V = 41,560 µm3
Vcs = 611,341 µm3
3D XRM
L = 107.6 µm
I = 63.5 µm
S = 21.6 µm
M = 107.8 µm
Dis = 21.6 µm
Dcs = 108.6 µm
A = 13,022 µm2
V = 53,606 µm3
Vcs = 656,474 µm3

Table 1.—*Common shape factors (after Blott and Pye, 2008). Abbreviations: L = long axis; I = intermediate axis; S = short axis; V = volume of the particle; Vcs = volume of the circumscribed sphere; M = maximum axis length; A = surface area of the particle; Dis = diameter of the largest inscribed sphere; Dcs = diameter of the smallest circumscribed sphere; Dr = diameter of the curvature of the particle corners; n = number of corners of the particle.*

Shape factors	Formula	Range	Application
Wentworth flatness index *Wentworth (1922)*	$\frac{L+I}{2S}$	1 to +∞	Flatness index: 1 = cubic or spherical particle +∞ = flat particle
Corey shape factor *Corey (1949)*	$\frac{S}{\sqrt{LI}}$	0 to 1	Flatness index: 0 = flat particle 1 = cubic or spherical particle
Janke form factor *Janke (1966)*	$\frac{S}{\sqrt{\frac{L^2+I^2+S^2}{3}}}$	0 to 1	Flatness index: 0 = flat particle 1 = cubic or spherical particle
Aschenbrenner shape factor *Aschenbrenner (1956)*	$\frac{LS}{I^2}$	0 to +∞	Oblate-Prolate index: 0 to 1 = oblate particle 1 = spherical particle 1 to +∞ = prolate particle
Williams shape factor *Williams (1965)*	$1-\frac{LS}{I^2}$, when $I^2 > LS$, $\frac{I^2}{LS}-1$, when $I^2 \leq LS$	-1 to +1	Oblate-Prolate index: 0 to +1 = oblate particle 0 to -1 = prolate particle
Oblate-Prolate Index *Dobkins and Folk (1970)*	$\frac{10\left(\frac{L-I}{L-S}-0.5\right)}{\frac{S}{L}}$	-∞ to +∞	Oblate-Prolate index: 0 to +∞ = prolate particle 0 to -∞ = oblate particle
Krumbein intercept sphericity *Krumbein (1941)*	$\sqrt[3]{\frac{IS}{L^2}}$	0 to 1	Sphericity index: 0 = non-spherical particle 1 = spherical particle
Maximum projection sphericity *Folk (1955)*	$\sqrt[3]{\frac{S^2}{LI}}$	0 to 1	Sphericity index: 0 = non-spherical particle 1 = spherical particle
Aschenbrenner working sphericity *Aschenbrenner (1956)*	$\frac{12.8\sqrt[3]{P^2Q}}{1+P(1+Q)+6\sqrt{1+P^2(1+Q^2)}}$, where $P=\frac{S}{I}$ and $Q=\frac{I}{L}$	0 to 1	Sphericity index: 0 = non-spherical particle 1 = spherical particle
Degree of true sphericity *Wadell (1932)*	$\frac{s}{A}=\frac{\sqrt[3]{36\pi V^2}}{A}$	0 to 1	Sphericity index: 0 = non-spherical particle 1 = spherical particle
Operational sphericity *Wadell (1933), Aschenbrenner (1956)*	$\sqrt[3]{\frac{V}{Vcs}}=\sqrt[3]{\frac{V}{\frac{4}{3}\pi(\frac{M}{2})^3}}$	0 to 1	Sphericity index: 0 = non-spherical particle 1 = spherical particle
Inscribed circle sphericity *Riley (1941)*	$\sqrt{\frac{Dis}{Dcs}}$	0 to 1	Sphericity index: 0 = non-spherical particle 1 = spherical particle
Wadell roundness *Wadell (1932) first formula*	$\frac{(\frac{\sum Dr}{n})}{Di}$	0 to 1	Roundness index: 0 = angular particle 1 = rounded particle

Table 2.—*Average shape parameters measured and standard deviations for gold grain 1. These results are based on five meshes produced with the five measurements in Fig. 2, for the SEM method, and on three meshes produced with different apparent density, for the XRM method. The differences between the estimates with the two methods are expressed for gold grains 1 to 4.*

	Gold Grain 1			**Gold Grain 2**	**Gold Grain 3**	**Gold Grain 4**
Shape parameters	*3D XRM*	*3D SEM*	*Difference*	*Difference*	*Difference*	*Difference*
L (µm)	283.5 ± 0.9	297.0 ± 6.2	**4.8 %**	11.6 %	**1.9 %**	**2.1 %**
I (µm)	175.7 ± 0.2	174.9 ± 3.8	**0.5 %**	16.6 %	**0.2 %**	**2.8 %**
S (µm)	124.7 ± 0.6	123.3 ± 2.6	**1.1 %**	**6.9 %**	**0.8 %**	21.8 %
M (µm)	300.4 ± 0.6	301.6 ± 6.3	**0.4 %**	**3.7 %**	**9.2 %**	**2.6 %**
Dis (µm)	123.4 ± 0.7	123.3 ± 2.8	**0.1 %**	**3.3 %**	**1.8 %**	22.2 %
Dcs (µm)	301.1 ± 0.8	305.2 ± 6.4	**1.4 %**	10.2 %	**1.9 %**	**2.8 %**
A ($µm^2$)	1.4E+05 ± 6.8E+02	1.3E+05 ± 5.6E+03	**1.7 %**	**7.5 %**	27.2 %	10.2 %
V ($µm^3$)	2.9E+06 ± 6.2E+04	3.1E+06 ± 1.9E+05	**5.9 %**	24.2 %	42.9 %	22.5 %
Vcs ($µm^3$)	1.4E+07 ± 7.9E+04	1.4E+07 ± 8.9E+05	**1.3 %**	11.5 %	**1.9 %**	**6.9 %**

Table 3.—*Average shape factors computed for grain 1 and the differences between the two methods expressed for gold grains 1 to 4.*

	Gold Grain 1			**Gold Grain 2**	**Gold Grain 3**	**Gold Grain 4**
Shape factors	*3D XRM*	*3D SEM*	*Difference*	*Difference*	*Difference*	*Difference*
Degree of flatness (S/I)	0.71	0.70	**1.4 %**	**9.2 %**	**0.0 %**	23.5 %
Degree of elongation (I/L)	0.62	0.59	**4.8 %**	**5.1 %**	**1.3 %**	**5.1 %**
Degree of equancy (S/L)	0.44	0.42	**4.5 %**	**5.0 %**	**2.0 %**	20.0 %
Wentworth flatness index	1.84	1.91	**3.8 %**	**6.0 %**	**0.0 %**	27.5 %
Corey shape factor	0.56	0.54	**3.6 %**	**6.0 %**	**0.0 %**	23.1 %
Janke form factor	0.61	0.58	**4.9 %**	**5.4 %**	**0.0 %**	23.3 %
Aschenbrenner shape factor	1.15	1.20	**4.3 %**	11.6 %	**3.3 %**	27.6 %
Williams shape factor	-0.13	-0.16	23.1 %	220.0 %	30.0 %	38.1 %
Oblate-Prolate Index	4.07	4.89	20.1 %	675.9 %	294.4 %	562.5 %
Krumbein intercept sphericity	0.65	0.63	**3.1 %**	**0.0 %**	**1.4 %**	**6.1 %**
Maximum projection sphericity	0.68	0.66	**2.9 %**	**3.9 %**	**0.0 %**	14.6 %
Aschenbrenner working sphericity	0.87	0.86	**1.1 %**	**1.1 %**	**0.0 %**	10.8 %
Degree of true sphericity	0.72	0.76	**5.6 %**	**6.7 %**	75.0 %	**5.7 %**
Operational sphericity	0.59	0.60	**1.7 %**	**2.9 %**	13.7 %	**4.7 %**
Inscribed circle sphericity	0.64	0.64	**0.0 %**	**4.1 %**	**0.0 %**	11.1 %
Wadell roundness	0.47	0.43	**8.5 %**	19.6 %	100.0 %	100.0 %

Table 4.—*Comparison of shape parameters and computed shape factors between 2D SEM and 3D SEM, for gold grain 1. Dis and Dcs are estimated in 2D based on the diameter of the largest inscribed circle and the smallest circumscribed circle, respectively.*

Shape parameters and factors	*2D SEM*	*3D SEM*	*Difference*
L (µm)	289	297.0	2.7 %
I (µm)	135	174.9	22.8 %
S (µm)	54	123.3	56.2 %
M (µm)	Non-measurable	301.6	Non-measurable
Dis (µm)	171	123.3	38.7 %
Dcs (µm)	295	305.2	3.3 %
A (μm^2)	Non-measurable	134386	Non-measurable
V (μm^3)	Non-measurable	3071205	Non-measurable
Vcs (μm^3)	Non-measurable	14376811	Non-measurable
Degree of flatness (S/I)	0.40	0.70	42.9 %
Degree of elongation (I/L)	0.47	0.59	20.3 %
Degree of equancy (S/L)	0.19	0.42	54.8 %
Wentworth flatness index	3.93	1.91	105.8 %
Corey shape factor	0.27	0.54	50.0 %
Janke form factor	0.29	0.58	50.0 %
Aschenbrenner shape factor	0.86	1.20	28.3 %
Williams shape factor	0.14	-0.16	187.5 %
Oblate-Prolate Index	8.31	4.89	69.9 %
Krumbein intercept sphericity	0.44	0.63	30.2 %
Maximum projection sphericity	0.42	0.66	36.4 %
Aschenbrenner working sphericity	0.66	0.86	23.3 %
Degree of true sphericity	Non-estimated	0.76	Non-estimated
Operational sphericity	Non-estimated	0.60	Non-estimated
Inscribed circle sphericity	0.76	0.64	18.8 %
Wadell roundness	0.41	0.43	4.7 %